A Model Study of the Spectral Structure of Boundary-Driven Rossby Waves and Related Altimetric Implications

STEFANO PIERINI

Istituto di Meteorologia e Oceanografia, Università di Napoli "Parthenope," Naples, Italy

(Manuscript received 12 September 2003, in final form 4 August 2004)

ABSTRACT

A two-layer primitive equation box model of the North Pacific Ocean is used to highlight and analyze some general aspects of the linear large-scale boundary-driven oceanic variability that are detectable through altimeter observations. The model is forced by a white-noise wind, and a spectral analysis of the zonal and meridional, barotropic and baroclinic velocity components is carried out. Several dynamical features are identified in terms of boundary-driven Rossby waves, and their spatial structure and frequency dependence are examined theoretically and discussed in connection with recent studies based on altimeter data. In particular, the following aspects of the variability are analyzed: 1) beta-refracted baroclinic Rossby waves, which are found to be generated along the eastern boundary of the ocean by the passage of coastal Kelvin waves originating from the equatorial waveguide, and 2) westward-intensified barotropic Rossby waves, which originate from the western boundary of the ocean after reflection of longer waves generated in midocean. In the discussion the stress is put on dynamical aspects not yet fully understood and on the possibility that altimetry can provide further insight into their functioning.

1. Introduction

The synoptic monitoring of the geostrophic surface variability and the detection of the barotropic variability in the oceans are among the most significant applications of microwave altimetry to physical oceanography. Before the advent of this remote sensing technique the surface dynamic height could be mainly determined indirectly through sparse hydrographic measurements or by means of alternative in situ or Lagrangian measuring procedures, and it was hard to follow the temporal variations, especially at the seasonal or shorter time scales. The knowledge of the barotropic variability was, on the other hand, even more difficult to achieve, as the barotropic signal is transparent to the thermal wind relationship. Despite the large number of studies based on altimeter data and devoted to analyzing aspects related to these problems [e.g., see Fu and Chelton (2001) and Picaut and Busalacchi (2001) for a review], some relevant dynamical features are still waiting to be considered in a systematic way, among which are the spectral and spatial properties of the large-scale oceanic variability associated with Rossby waves radiating from the coasts of the continents (which will be denoted here as "boundary driven" Rossby waves). In this context, both baroclinic and barotropic boundary-driven Rossby waves will be analyzed in this paper through a numerical process study.

For baroclinic waves, it has been recognized that westward-propagating boundary-driven baroclinic Rossby waves of periods from a few months to years radiate from the eastern boundaries of the oceans, where they are generated either by local fluctuating winds or by poleward-propagating coastal Kelvin waves originating from variable winds in the equatorial waveguide (e.g., White 1977; Meyers 1979; White and Saur 1981; Chelton and Davis 1982; Cummins et al. 1986; Herrmann and Krauss 1989; Johnson and O'Brien 1990a,b; Chelton and Schlax 1996; Qiu et al. 1997; White et al. 1998; Soares et al. 1999; Kelly and Thompson 2002; Fu and Qiu 2002). The predominant generating mechanism for waves associated with El Niño events was attributed long ago to coastal Kelvin waves of equatorial origin, as described by the illuminating theoretical studies of Anderson and Rowlands (1976) and McCreary (1976). A recent model study (Pierini 2003) showed that the interpretation of boundary-driven baroclinic Rossby waves of annual period in the Pacific in terms of equatorially controlled waves is consistent with altimeter observations. Because of the dependence of Rossby wave speed with latitude, peculiar wave patterns and a longitudinal confinement of the sea surface height (SSH) variability are produced through a dynamical mechanism usually denoted as "beta refrac-

Corresponding author address: Stefano Pierini, Istituto di Meteorologia e Oceanografia, Università di Napoli "Parthenope," Via A. De Gasperi, 5 - 80133 Napoli, Italy.
E-mail: stefano.pierini@uniparthenope.it

© 2005 American Meteorological Society

tion," which was studied analytically by Schopf et al. (1981). This effect was revealed synoptically by Ocean Topography Experiment (TOPEX)/Poseidon (T/P) and *European Remote Sensing Satellite* (*ERS*)*-1–2* data analyses (e.g., Chelton and Schlax 1996; White et al. 1998; Fu and Qiu 2002; Kelly and Thompson 2002). However, a systematic and quantitative study based on altimeter data specifically devoted to analyzing beta-refracted boundary-driven baroclinic Rossby waves appears to be still lacking, and yet it could provide valuable information on the oceanic variability, particularly in tropical oceans. To this respect, a theoretical study aimed at analyzing the main spectral features of this part of the variability could be useful for further experimental studies.

For barotropic Rossby waves, they are known to be generated by the wind mainly at mid- and high latitudes. They have relatively small periods [$O(100)$ days or less] and their highest frequency band is not even resolved by the T/P data (that have a 20-day Nyquist period). Nonetheless, evidence of barotropic Rossby wave variability in T/P data is available both for the resolved longer period part of the spectrum (e.g., Kobashi and Kawamura 2001) and for the aliased, smaller period signals (Stammer et al. 2000). In the analysis of Kobashi and Kawamura (2001) evidence is given of Rossby waves compatible with the barotropic dispersion relation, whose amplitude is large off the western boundary in the Pacific Subtropical Countercurrent region, and decreases as the distance from the boundary increases. Can this effect be explained in terms of boundary-driven barotropic Rossby waves? Pedlosky (1987) showed that long westward-propagating barotropic Rossby waves generated in midocean by wind fluctuations are reflected at the western boundary of the ocean as short waves, whose energy propagates eastward. Damping effects can then produce a sort of westward intensification and confinement of the wave field (Pierini 1998). A theoretical study of this nature could provide a useful basis for an interpretation of this part of the barotropic variability as revealed in altimeter data.

In this framework, a modeling process study of the spectral and spatial properties of the linear large-scale wind-driven oceanic variability associated with baroclinic and barotropic boundary-driven Rossby waves is presented in this paper. The aim is to provide theoretical tools that could be useful in interpreting, through altimeter data, beta-refracted Rossby waves radiating from the eastern boundaries and barotropic Rossby waves radiating from the western boundaries of the oceans. The paper is organized as follows. In section 2 the modeling process study (based on a spectroscopic analysis of the zonal and meridional, barotropic and baroclinic velocity components produced by a two-layer primitive equation box model of the North Pacific Ocean) is described, and the numerical results are summarized. In section 3a a detailed discussion of the numerical results is given for beta-refracted baroclinic Rossby waves radiating from the eastern boundary, while in section 3b their experimental evidence, mainly from altimeter data, is discussed. In section 4, barotropic Rossby waves reflected at the western boundary are discussed, both on the basis of numerical and experimental results. Last, in section 4 conclusions are drawn.

2. Summary of the numerical results

The mathematical model and the setup adopted in the present study are the same used by Pierini (2003) for a process study of the seasonal variability in the tropical North Pacific Ocean (the reader should therefore refer to that paper for the details); here we summarize the main features of the model. A two-layer primitive equation flat-bottom, shallow-water model is solved through an explicit leapfrog algorithm, with spatial and temporal steps given by (x and y are the zonal and meridional coordinates, respectively) $\Delta x = 100$ km, $\Delta y = 111$ km (so that one grid step corresponds to 1° in latitude) and $\Delta t = 135$ s. The integration domain is a box covering the latitudinal range $\varphi = 30°$S–52°N; therefore it is a rectangle of meridional length $L_y = 9102$ km, and with a zonal length $L_x = 9000$ km representing a rough meridional mean value of the Pacific zonal width. Along y the Coriolis parameter $f = 2\Omega_{\text{earth}} \sin\varphi$ models correctly the Coriolis force as a function of latitude. The following parameter values are chosen ($i = 1, 2$ stands for upper and lower layer, respectively): $D_1 = 200$ m and $D_2 = 3800$ m are the undisturbed layer depths, $\rho_1 = 1.026$ g cm^{-3} and $\rho_2 = 1.028$ g cm^{-3} are the layer densities, and $A_H = 1000$ m^2 s^{-1} is the lateral eddy viscosity coefficient. Except for the wind forcing and for a smaller value of the viscosity coefficient, the only difference between the model of Pierini (2003) and the present one is that now the equations are linearized. Nonlinearities were already found to be negligible in such a coarse-resolution model, but now nonlinear terms are explicitly neglected because this is required in principle for a spectral analysis like the one performed here. In this study the following variables are used: H_i are the layer depths and u_i and v_i are the zonal and meridional velocity components, respectively.

Since a spectral analysis is to be performed, the linear system is forced by a *white-noise* zonal wind stress (the meridional wind stress being taken equal to zero) of the form (Pierini 1996, 1997)

$$\tau_{\text{zonal}}(\mathbf{x}, t) = \tau_0(\mathbf{x}) \frac{1}{N} \sum_{k=1}^{N} \sin(\omega_k t), \tag{1}$$

where $\omega_1 = 2\pi/T_{\max}$, $\omega_N = 2\pi/T_{\min}$, and $\omega_k = (k - 1)(\omega_N - \omega_1)/(N - 1) + \omega_1$, with $N = 1000$, $T_{\min} = 5$ days, and $T_{\max} = 500$ days, so as to cover a broad range of periods that include the seasonal variability up to the smallest subinertial time scales [in the following we will refer to the frequencies $\nu_k = \omega_k/(2\pi)$]. As for the choice of $\tau_0(\mathbf{x})$, the aim is to reveal in the clearest way possible

the oceanic response to different forcing frequencies, and this can be best achieved through the use of the simplest possible (though dynamically nontrivial) wind field. In a basic numerical experiment (experiment 1) a wind with constant curl is therefore chosen (Fig. 1):

$$\tau_0 = \chi(y - y_0)/L_y, \tag{2}$$

where $y_0 = L_y/2$ [with $\varphi = 30°$S for $y = 0$ this corresponds to vanishing winds at $\varphi_0 \equiv \varphi(y_0) = 11°$N] and $\chi = 0.005$ N m^{-2} (in view of the linearity of the model this last parameter is arbitrary). In a second numerical experiment (experiment 2; Fig. 1) the winds vanish at the equator ($\varphi_0 = 0°$)—that is, $y_0 = 3330$ km (this will allow us to assess that the baroclinic Rossby waves radiating from the eastern boundary are generated remotely in the equatorial waveguide). In experiment 3 the wind along the meridional boundaries is set to zero through the following position:

$$\tau_0 = [\chi(y - y_0)/L_y] \sin(\pi x/L_x), \tag{3}$$

where, again, $y_0 = L_y/2$ (this will allow us to assess that the Rossby waves seen to be radiating from the meridional boundaries are not generated by locally fluctuating winds). Last, in experiment 4, experiment 1 is run with a higher eddy viscosity coefficient, $A_H = 10\,000$ m^2 s^{-1} (this will show that the spatial structure of the baroclinic signal is independent on A_H, but that the barotropic signal does depend on it). See Table 1 for a summary of the experiments.

Because the oceanic response is basically in the form of baroclinic and barotropic Rossby and Kelvin waves, the best way to identify them is to decompose the wind-driven velocity in a barotropic component (defined here as the vertically averaged velocity) and a baroclinic component and to analyze them separately. The barotropic velocities $\mathbf{u}_{\rm btp}$ are thus given by

$$\begin{aligned} u_{\rm btp} &= (u_1H_1 + u_2H_2)/(H_1 + H_2) \quad \text{and} \\ v_{\rm btp} &= (v_1H_1 - q_{\rm Ekman} + v_2H_2)/(H_1 + H_2)\,, \end{aligned} \tag{4}$$

where the meridional Ekman (volume) transport $q_{\rm Ekman} = -\tau_{\rm zonal}/\rho_1 f$ is subtracted from the meridional upper-layer transport because, as we are interested in applications to altimeter data, only velocities that produce a geostrophically balanced signal in the SSH must be considered. The baroclinic velocity in the upper layer (the interesting one in altimeter applications) $\mathbf{u}_{\rm 1bcl} \equiv \mathbf{u}_{\rm bcl}$ will then be given by

$$\begin{aligned} u_{\rm bcl} &= u_1 - u_{\rm btp} \quad \text{and} \\ v_{\rm bcl} &= v_1 - \frac{q_{\rm Ekman}}{H_1} - v_{\rm btp}\,. \end{aligned} \tag{5}$$

The experimental subsurface velocity $\mathbf{u}_{\rm altimeter}$ that can be obtained from the dynamically active altimeter SSH through the geostrophic relation has its counterpart in our numerical velocity $\mathbf{u}_{\rm surface} = \mathbf{u}_{\rm btp} + \mathbf{u}_{\rm bcl}$.

Each experiment consists of a run of $t = 1024$ days, and the fast Fourier transform of the velocities is then computed in each point x at every 5° in latitude, ending up with the quantities $\tilde{u}_{\rm btp}(\mathbf{x}, \nu)$, $\tilde{v}_{\rm btp}(\mathbf{x}, \nu)$, $\tilde{u}_{\rm bcl}(\mathbf{x}, \nu)$, and $\tilde{v}_{\rm bcl}(\mathbf{x}, \nu)$. The results concerning experiment 1 are reported in Figs. 2, 3, 4, and 5: they will be discussed in the next section, while their content is outlined below. In Figs. 2a–c, the logarithm of the spectral density of the baroclinic zonal velocities, $\log_{10} |\tilde{u}_{\rm bcl}(x, \hat{y}_k, \nu)|$ [$\hat{y}_k \equiv y(\varphi_k)$], is shown as a function of x and ν at the latitudes $\varphi_1 = 5°$N, $\varphi_2 = 10°$N, and $\varphi_3 = 15°$N, while in Figs. 2d–f, the same quantities but for the meridional component $\tilde{v}_{\rm bcl}$ are given. In Fig. 3 a snapshot, at $t = 428$ days, of the interface displacement of the model response to a single-frequency wind forcing ($\nu = 0.0075$ cycles day^{-1}, from now on "cpd") with the same parameters of experiment 1 is shown. To obtain gross

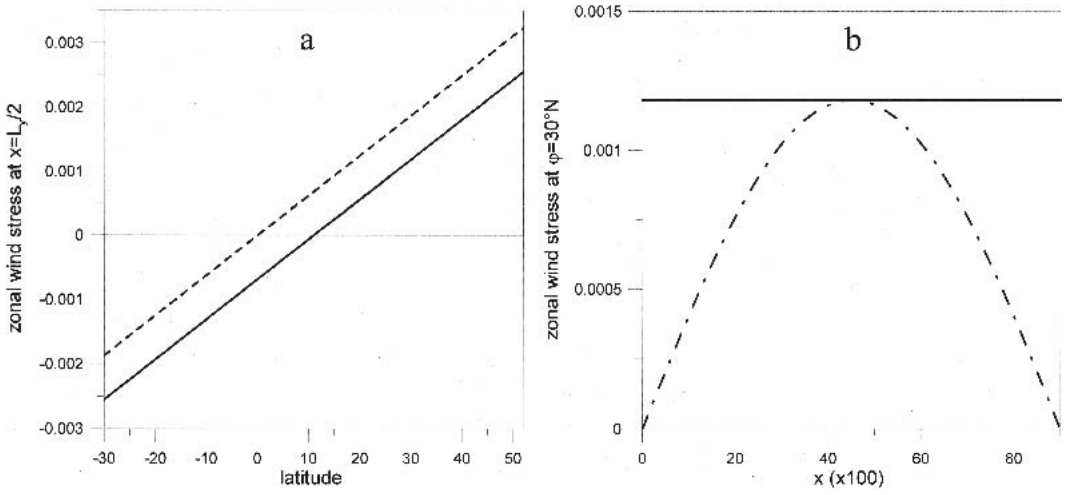

FIG. 1. (a) Meridional profile of τ_0 at $x = L_y/2$ for expts 1, 3, and 4 (solid line) and for expt 2 (dashed line); (b) zonal profile of τ_0 at $\varphi = 30°$N for expts 1, 2, and 4 (solid line) and for expt 3 (dotted–dashed line). Units: N m^{-2}.

TABLE 1. Summary of the numerical experiments. For the exact definition of the zonal and meridional dependence of the zonal wind stress τ_0 see section 2.

Expt	Lat (°N) at which τ_0 vanishes	Zonal dependence of τ_0	A_H (m^2 s^{-1})
1	$\varphi_0 = 11°$	Constant	1000
2	$\varphi_0 = 0°$	Constant	1000
3	$\varphi_0 = 11°$	Sinusoidal [Eq. (3)]	1000
4	$\varphi_0 = 11°$	Constant	10 000

information on the dependence of the various spectral densities upon the latitude, zonally and frequency-integrated quantities are constructed:

$$Q_j(\tilde{\zeta}, \varphi) = \log_{10}\left\{\int_0^{L_x}\int_{\nu_j}^{\nu_{j+1}} |\tilde{\zeta}[x, y(\varphi), \nu]|\, dx\, d\nu\right\}. \quad (6)$$

The variable $\tilde{\zeta}$ can be any of the four quantities $\tilde{u}_{\rm btp}$, $\tilde{v}_{\rm btp}$, $\tilde{u}_{\rm bcl}$, or $\tilde{v}_{\rm bcl}$, and the frequencies ν_j are $\nu_1 = 0$ cpd, $\nu_2 = 0.01$ cpd, $\nu_3 = 0.02$ cpd, $\nu_4 = 0.03$ cpd, $\nu_5 = 0.04$ cpd, $\nu_6 = 0.05$ cpd, and $\nu_7 = 0.06$ cpd. The functions $Q_j(\tilde{\zeta},\varphi)$ are shown in Figs. 4a–d. Moreover, in order to assess the relative importance of the baroclinic and barotropic, zonal and meridional velocity spectral densities, the quantities $[Q_j(\tilde{u}_{\rm btp}, \varphi) - Q_j(\tilde{u}_{\rm bcl}, \varphi)]$, $[Q_j(\tilde{v}_{\rm btp}, \varphi) - Q_j(\tilde{v}_{\rm bcl}, \varphi)]$, $[Q_j(\tilde{u}_{\rm btp}, \varphi) - Q_j(\tilde{v}_{\rm btp}, \varphi)]$, and $[Q_j(\tilde{u}_{\rm bcl}, \varphi) - Q_j(\tilde{v}_{\rm bcl}, \varphi)]$ are shown in Figs. 5a–d, respectively. Moreover, the logarithm of the spectral density of the baroclinic zonal velocities at $\varphi_1 = 5°$N, $\varphi_2 = 10°$N, and $\varphi_3 = 15°$N are shown in Figs. 6a–c for experiment 2, in Figs. 6d–f for experiment 3, and in Figs. 7a–c for experiment 4. The logarithm of the spectral density of the barotropic meridional velocities at $\varphi = 20°$N are shown in Figs. 8b–d for experiment 1, 3, and 4, respectively. Last, in Figs. 9a and 9b the same ratios of Figs. 5a and 5b are reported in the case in which the spatial integration in Eq. (6) is from $x = 500$ km to $x = L - 500$ km. The interpretation and discussion of these results will be the subject of the next sections.

3. Beta-refracted baroclinic Rossby waves radiating from the eastern boundary

In this section and in the next one the analysis of the numerical results will allow us to identify several as-

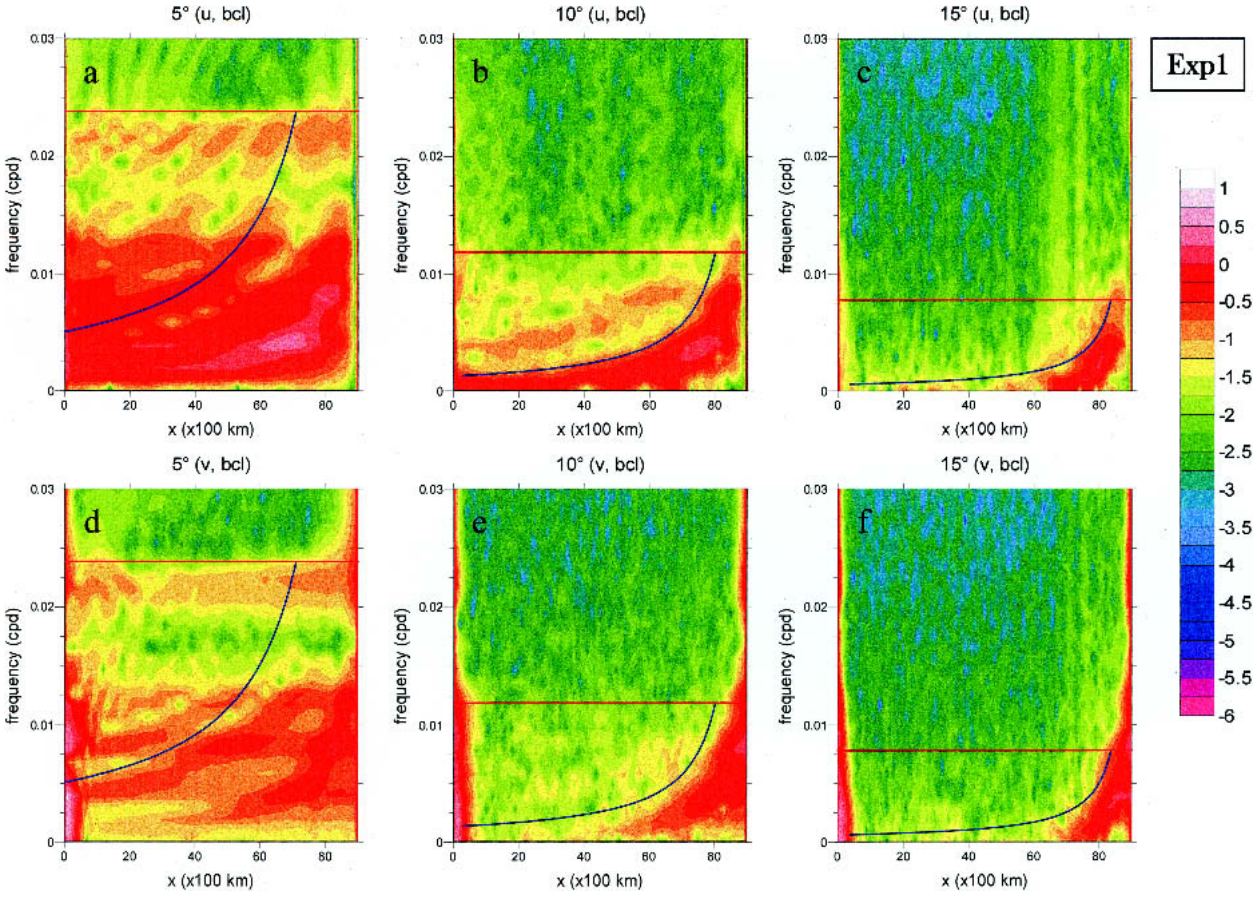

FIG. 2. Expt 1: longitude–frequency maps of $\log_{10}$ of the spectral density of the upper-layer baroclinic velocity at different latitudes. (a)–(c) Zonal component at 5°, 10°, and 15°N; (d)–(f) meridional component at 5°, 10°, and 15°N. For the red and blue lines see text (section 3a).

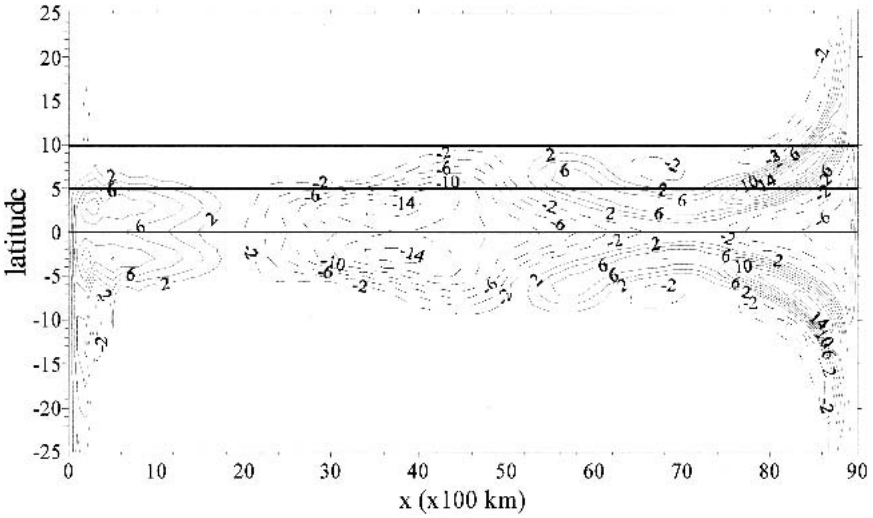

FIG. 3. Snapshot of the interface displacement (t = 428 days) of the model response to a single-frequency wind forcing (ν = 0.0075 cpd) with the same parameters of expt 1.

pects of the large-scale boundary-driven variability, which will then be discussed in detail. We start with the low-frequency part of the spectrum.

a. Numerical results and interpretation

In Fig. 2 the distribution of the spectral density in the baroclinic mode for experiment 1 is shown as a function of frequency at φ = 5°, 10°, and 15°N (at such low latitudes the response is basically baroclinic for frequencies lower than $\nu \sim$ 0.02–0.03 cpd, as shown in Figs. 4 and 5a–b). An eastward confinement of the signal is evident at all latitudes and is more and more pronounced as the latitude increases; moreover, energy is confined to lower and lower frequencies as the latitude increases. This is compatible with the generation of baroclinic Rossby waves at the eastern boundary and consequent refraction of wave packets toward the equator due to the variation of the beta effect with latitude [e.g., Schopf et al. (1981) or Philander (1990) for a theoretical account, and White (1977), Chelton and Schlax (1996), or White et al. (1998) for experimental evidence]. Let us pass to validate this hypothesis.

Is the baroclinic signal actually associated with Rossby waves radiating from the eastern boundary, and through what mechanism are they generated? McCreary (1976) showed that in an El Niño event eastward-propagating equatorial Kelvin waves are generated by wind variations (a weakening or even a reversal of the trade winds), and their arrival at the eastern boundary generates equatorial Rossby waves and poleward-propagating coastal Kelvin waves, which in turn produce westward-propagating Rossby waves along the eastern coasts [analogous conclusions were drawn by Anderson and Rowlands (1976)]. Recently Pierini (2003) showed through a process study that the same mechanism is active also for the annual signal, suggesting a predominant remote equatorial forcing, as opposed to a local generation by fluctuating winds along the coasts, as suggested in other studies of the seasonal variability. In the present analysis, which constitutes a generalization of the result of Pierini (2003) to a wide range of frequencies, both the coastal generation of the waves and their remote equatorial forcing is proved by experiment 2. The wind forcing of experiment 2 has the same wind stress curl as that of experiment 1; so, if the oceanic signal were a locally coherent response to the wind, then the two forcings should produce basically the same response. On the contrary, the baroclinic signal of experiment 2 is orders of magnitude smaller than that of experiment 1, as shown in Fig. 6a–c for the zonal baroclinic component (cf. with Figs. 2a–c , respectively, for expt 1).

Such a remarkable decrease in the energy can be explained, according to our hypothesis, as follows. In experiment 1, the zonal winds in the equatorial band are strong and flow, instantaneously, in the same direction north and south of the equator (see the solid line of Fig. 1a). The corresponding Ekman transport at the equator produces upwelling (easterly winds) or downwelling (westerly winds) events with consequent formation of eastward-propagating equatorial Kelvin waves and the triggering of the teleconnection mechanism described above. On the contrary, in experiment 2 weak zonal winds are antisymmetric around the equator (see the dashed line of Fig. 1a), and this does not allow for the formation of equatorial Kelvin waves in midocean. Only weak coastal Kelvin waves are generated by zonal winds near the eastern coasts, and this accounts for the weak signal present in Figs. 6a–c. Further evidence that the waves are not predominantly generated by winds

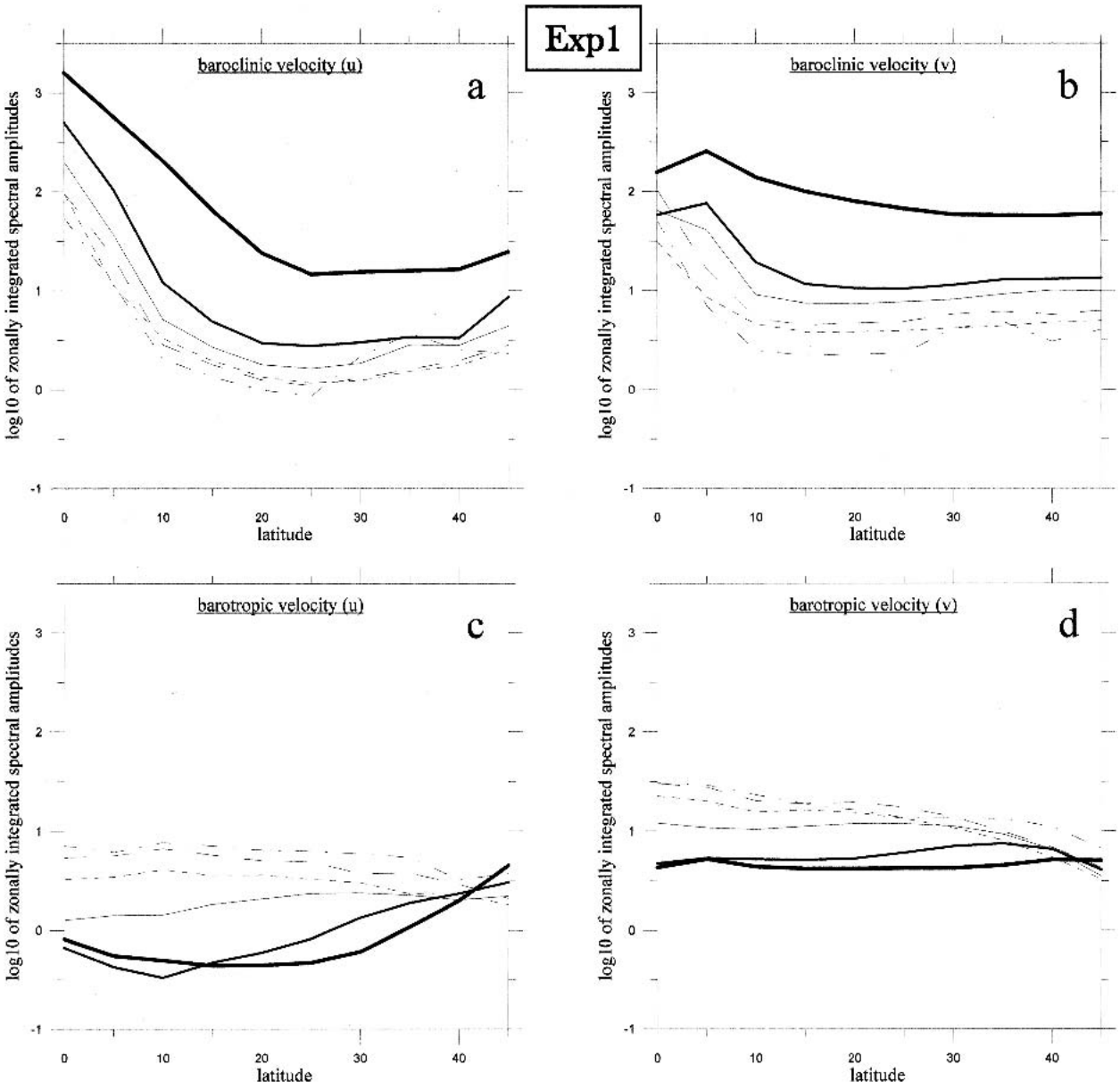

FIG. 4. Expt 1: $\log_{10}$ of the zonally and frequency integrated spectral densities as a function of latitude for the upper-layer baroclinic velocity [(a) zonal component, (b) meridional component] and for the barotropic velocity [(c) zonal component, (d) meridional component]. The six lines refer to different spectral bands over which integration has been performed (very thick solid: ν = 0–0.01 cpd; thick solid: ν = 0.01–0.02 cpd; solid: ν = 0.02–0.03 cpd; short dashed: ν = 0.03–0.04 cpd; long dashed: ν = 0.04–0.05 cpd; dashed–dotted: ν = 0.05–0.06 cpd).

along the coasts is provided by experiment 3 in which τ_0 (which now has the same latitudinal dependence as in expt 1) vanishes along the coast (dashed–dotted line of Fig. 1b), and yet the response is virtually unchanged with respect to that of experiment 1 (cf. Figs. 6d–f with Figs. 2a–c).

Incidentally, it should be noticed that since in experiments 1 and 2 the two wind forcings correspond to the same wind stress curl, the application of the quasigeostrophic equation to describe wave evolution would give the same result in both cases, namely the response of our primitive equations for experiment 2 (which is the one in which no Kelvin waves are active). This shows how inadequate the quasigeostrophic approximation is in describing the wind-driven oceanic variability in tropical regions, especially in the eastern part of the ocean, unless fluctuations associated to coastal Kelvin waves are prescribed as boundary conditions, as done, for instance, by Fu and Qiu (2002; see section 3b for more details).

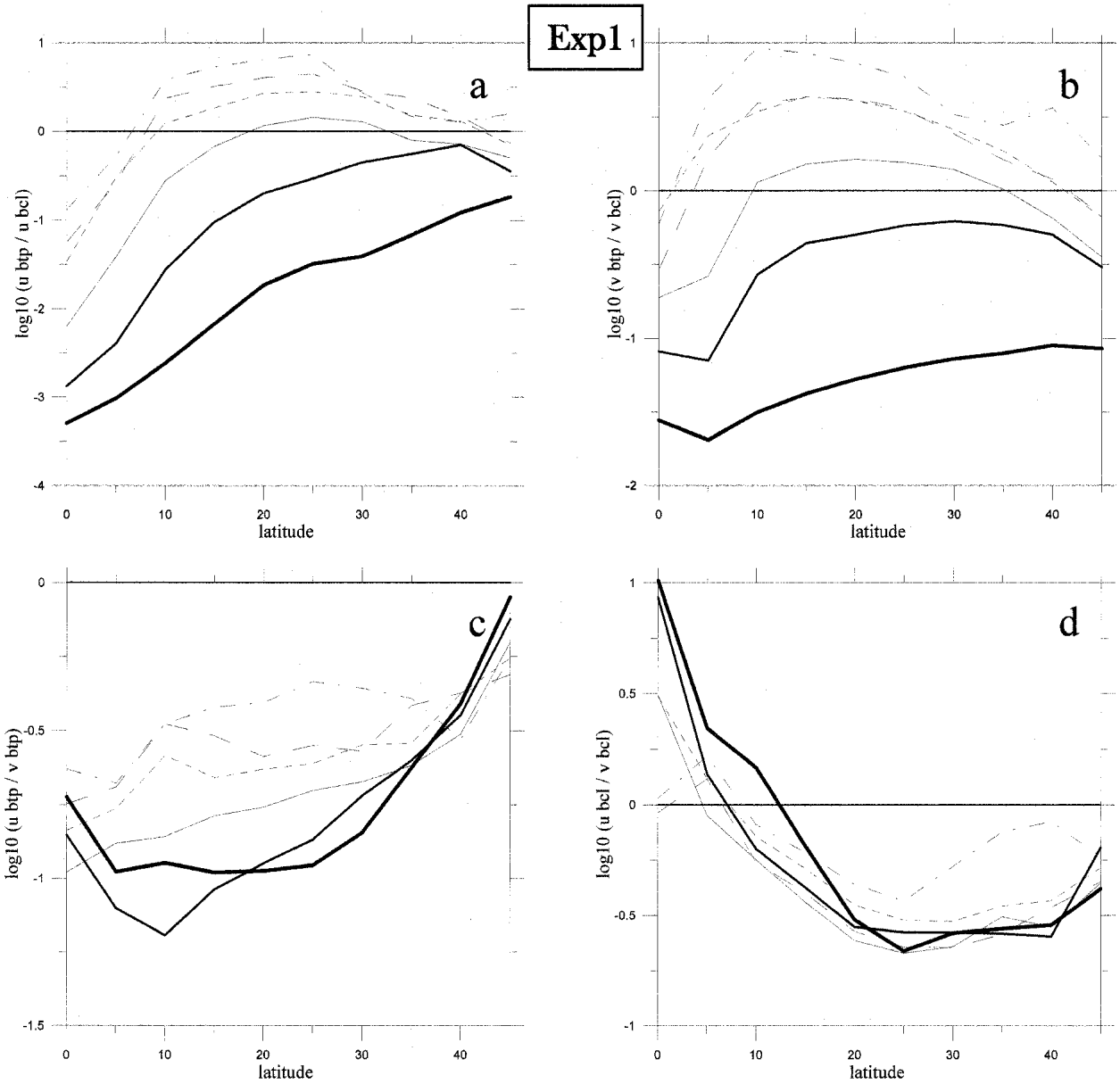

FIG. 5. Expt 1: $\log_{10}$ of the ratio between the zonally and frequency integrated spectral densities of the barotropic velocity and that of the upper-layer baroclinic velocity [(a) zonal component, (b) meridional component]; $\log_{10}$ of the ratio between the zonally and frequency integrated spectral densities of the zonal velocity and that of the meridional velocity [(c) barotropic velocities, (d) upper-layer baroclinic velocities]. For the definition of the six lines see Fig. 4.

How can one characterize quantitatively the beta-refraction of Rossby waves? Although a ray theory of beta dispersion of low-frequency Rossby waves propagating from meridional and sloping coastlines was developed long ago by Schopf et al. (1981), it is rather surprising that in recent studies of the tropical variability based on altimeter data, in which beta-refracted waves clearly emerge (see section 3b), no application of those theoretical results appears to have been made. Besides Schopf et al. (1981), we believe that Philander and Yoon (1982) proposed a simple, yet powerful, criterion to determine the shape of beta-refracted wave patterns that could be used in interpreting the altimeter-derived oceanic variability in the eastern tropical oceans, and that we are now going to test in our numerical study.

By studying the adjustment of an inviscid ocean at an eastern coastal zone, Philander and Yoon (1982) showed that the offshore scale of the response produced by fluctuating alongshore winds (but the present case is equivalent) is the internal Rossby radius of deformation R_i $[=(g'\overline{D})^{1/2}/f$, where $\overline{D} = D_1D_2/(D_1 + D_2)]$

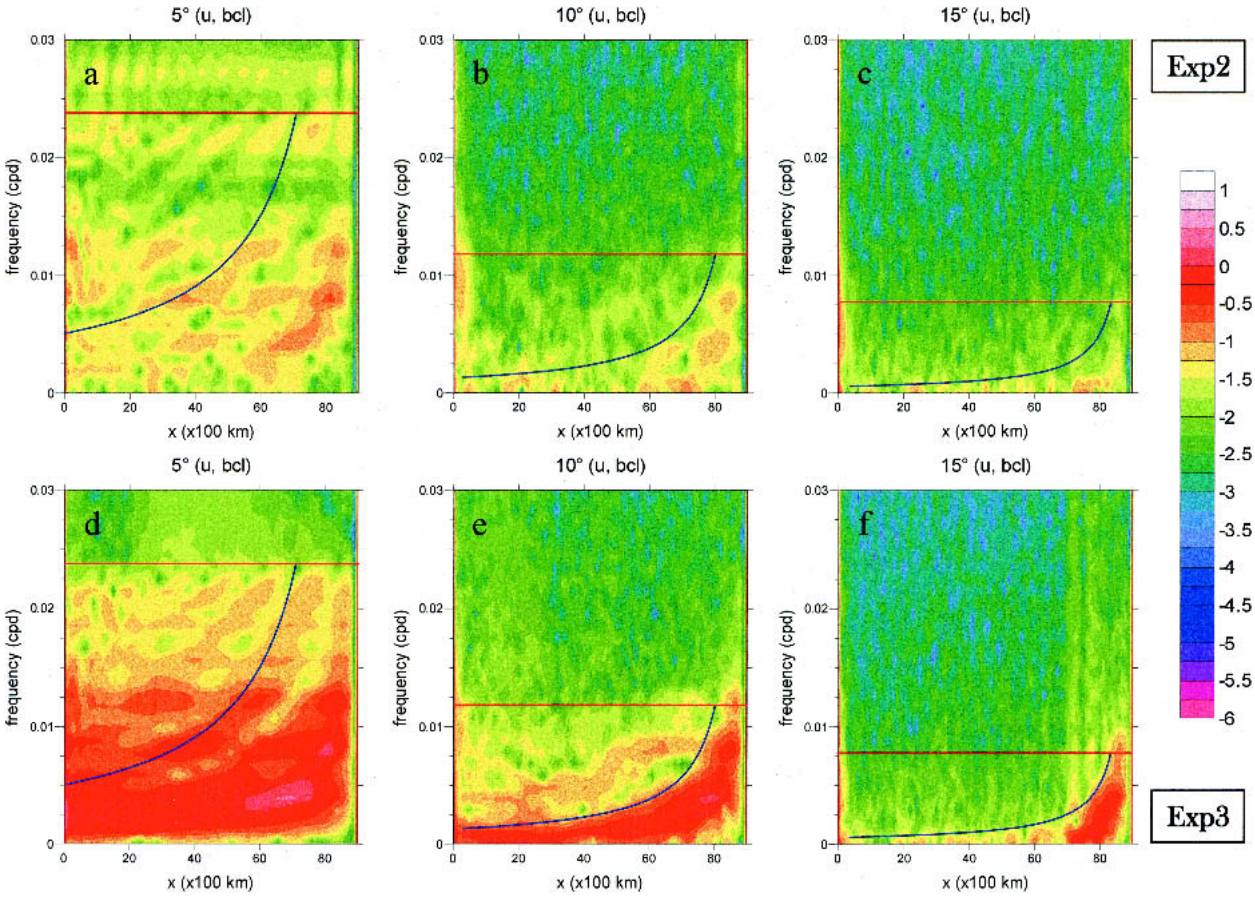

FIG. 6. Longitude–frequency maps of $\log_{10}$ of the spectral density of the zonal component of the upper-layer baroclinic velocity at 5°, 10°, and 15°N for (a)–(c) expt 2 and for (d)–(f) expt 3.

for forcing frequencies higher than the Rossby cutoff frequency,

$$\bar{\nu} = \beta R_i / 4\pi \tag{7}$$

(the maximum frequency for which Rossby waves can exist at that latitude), while, for lower forcing frequencies, it is equal to the distance covered by a Rossby wave during a period, that is, to the wavelength for that frequency. In Fig. 2 (and in Figs. 6 and 7) the blue lines, given by

$$\tilde{x} = L_x - \frac{\beta R_i^2}{\nu} \tag{8}$$

($x = L_x$ corresponds to the eastern boundary), represent the western limit of the low-latitude, beta-refracted Rossby waves according to this theory, while the horizontal red lines show the cutoff frequency $\bar{\nu}$ at each latitude according to (7), above which the offshore length scale should be given by the Rossby radius of deformation. The frequency-dependent shadow zone obtained in the numerical simulations agrees very well with the theoretical one delimited by the western and northern limits according to (7) and (8) at latitudes $\varphi = 10°$ and $\varphi = 15°$ (for $\varphi = 5°$, see below), as shown in Figs. 2b–f, but the agreement is evident at higher latitudes as well (figures not shown). For frequencies greater than $\bar{\nu}$ the variability along the eastern coast is mainly meridional (cf. Figs. 2e,f with Figs. 2b,c) and frequency independent, being due to coastal Kelvin waves (that have zero velocity normal to the coast), again in agreement with the findings of Philander and Yoon (1982). For our parameter values, $R_i(\varphi = 10°) \cong 76$ km and $R_i(\varphi = 15°) \cong 51$ km. The offshore extension of the signal is (Figs. 2e,f) slightly larger because of the coarse resolution of the model, which does not fully resolve the internal radius of deformation. Note, last, that also at the western boundary a strong confined signal is present (only in the meridional, i.e., alongshore, velocity component) in the form of coastal Kelvin waves propagating equatorward and deriving from high latitudes.

As several studies have clarified (Schopf et al. 1981; Philander 1990, his section 3.4.1), a Rossby wave packet that leaves a meridional coast with a purely zonal wavenumber ($k_y = 0$) will then be refracted toward the equator with a tendency for $|k_y|$ to increase, while k_x and ω

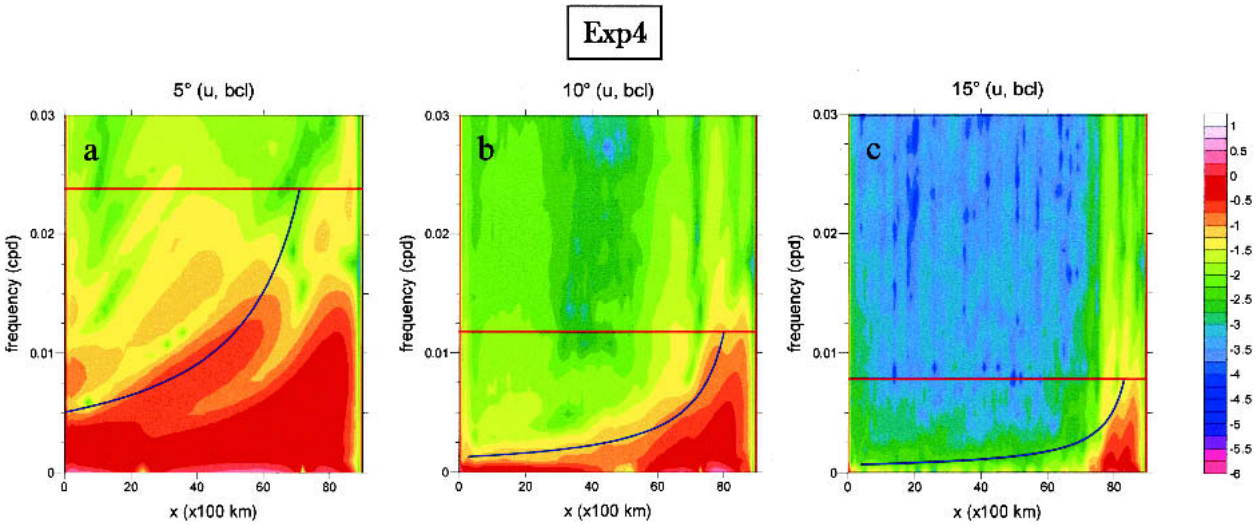

FIG. 7. Longitude–frequency maps of $\log_{10}$ of the spectral density of the zonal component of the upper-layer baroclinic velocity at (a) 5°, (b) 10°, and (c) 15°N for expt 4.

remain unchanged. In quasigeostrophic waves such as Rossby waves (for which the velocity is normal to the wavenumber vector), this implies that the ratio between the zonal and meridional components of the velocity increases rapidly as the equator is approached. This is perfectly compatible with the lines of Fig. 5d, where the logarithm of the ratio between the zonal and meridional velocity spectral densities is found to be much greater than unity for $\varphi < 10°$–15° (this being compatible with a predominant northward phase propagation) and much less than unity for $\varphi > 15°$ (this being compatible with a predominant westward phase propagation). This behavior can also be observed by comparing the zonal (Figs. 2b,c) and weaker meridional (Figs. 2e,f) velocity spectra at very low latitudes, by Figs. 4a and 4b, and by the snapshot of Fig. 3.

At $\varphi = 5°$ the energy distribution is consistent with the confinement expressed by (7) but not with that given by (8), as shown in Figs 2a and 2d; moreover, the baroclinic zonal spectral density at $\varphi = 10°$ (Fig. 2b) also shows a secondary, though weak, band of energy for longitudes west of the blue line. To understand the reason for this discrepancy the model has been run with the same parameters used for experiment 1, but with a monochromatic wind forcing. The forcing frequency is chosen as $\nu = 0.0075$ cpd so that for both $\varphi = 5°$ and $\varphi = 10°$ eastward confinement of the Rossby wave signal is expected according to (8) (see Figs. 2a,b,d,e). Figure 3 shows a snapshot of the interface displacement (at the arbitrary time of integration $t = 428$ days from the state of rest, but any other instant of time would provide the same information). The isolines show the typical beta-refracted Rossby wave patterns on the eastern side of the ocean [exhibiting a shadow zone west of about 1500 km from the eastern boundary at $\varphi = 10°$, as predicted by (8) and confirmed by Fig. 2b], but also a strong signal around the equator, which clearly accounts for the discrepancy under consideration. This is due to equatorial Kelvin and Rossby waves that, according to the theory of equatorially trapped waves (e.g., Philander 1990), have a latitudinal extension of 2–4 equatorial radii of deformation R_{eq}, where

$$R_{eq} = \left(\sqrt{g'\overline{D}}/\beta\right)^{1/2}.$$

In our case $R_{eq} \cong 290$ km, and so the equatorial disturbances are very strong at $\varphi = 5°$, thus deforming the refracted wave field and explaining the energy west of the blue line. On the other hand, also at $\varphi = 10°$ is some energy present in midocean, and this explains the secondary band of weak signal west of the blue line in Fig. 2b (note that, as shown in Fig. 3, the velocities are predominantly zonal there and this is the reason why energy confinement is better verified for the meridional component of the velocity, as reported in Fig. 2e).

Last, the theoretical arguments discussed in this section, and confirmed by the numerical results, are basically independent of any dissipative mechanism included in the model. However, it seems useful to stress this with an ad hoc numerical experiment. In experiment 4 all the parameters and wind forcing are the same as for experiment 1 except for the value of the lateral eddy viscosity coefficient, which now is chosen 10 times larger ($A_H = 10\,000$ m^2 s^{-1}). Figures 7a–c show that, apart for an obvious decrease in the amplitude of the response, the confinement is substantially the same as that produced in experiment 1 (cf. with Figs. 2a–c).

b. *Experimental evidence from altimeter data*

Let us now discuss experimental evidence of beta-refracted Rossby waves from altimeter data. Chelton

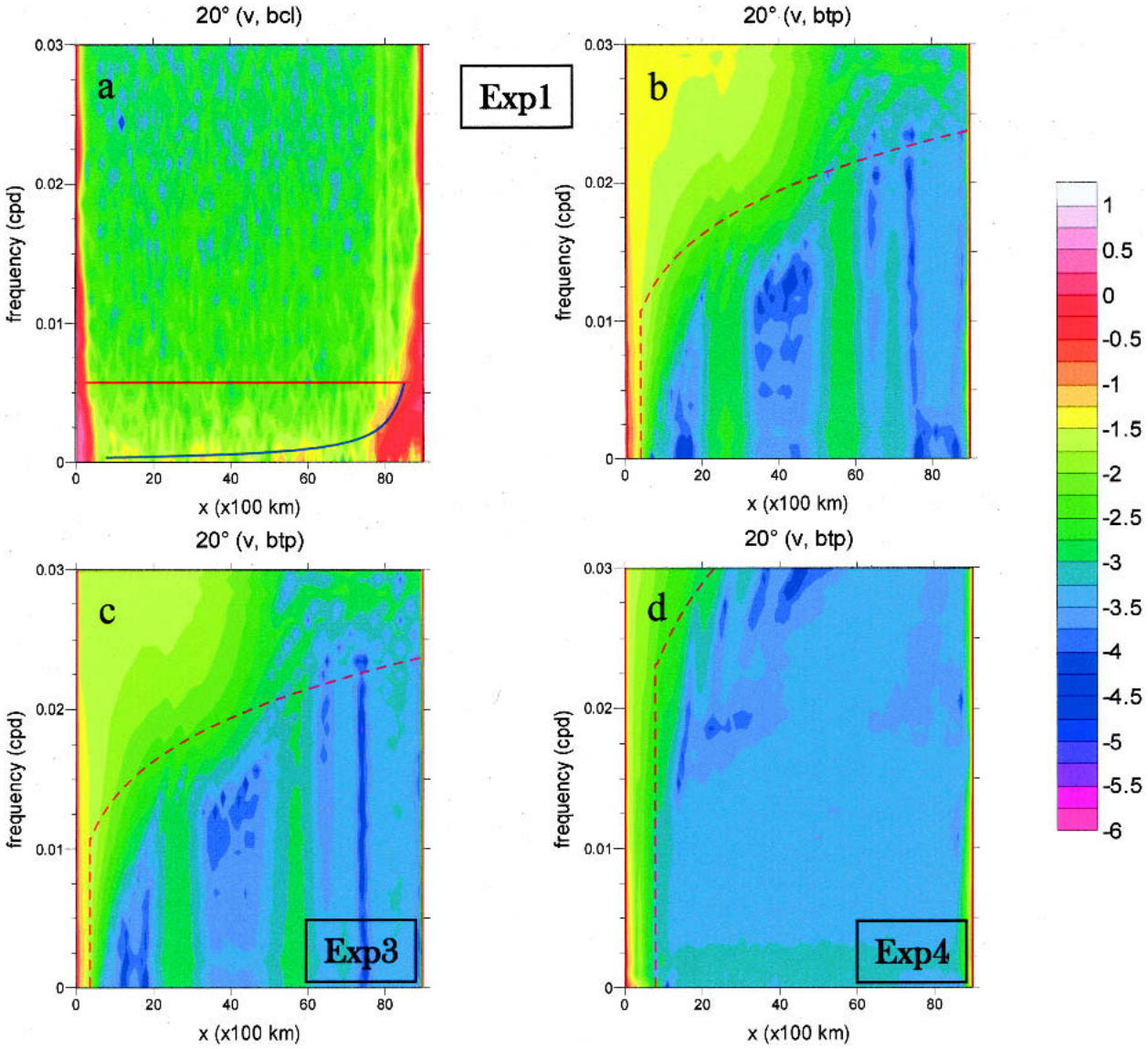

FIG. 8. Longitude–frequency maps of $\log_{10}$ of the spectral density of the meridional component of the upper-layer (a) baroclinic and (b) barotropic velocity at 20°N for expt 1. Longitude–frequency maps of $\log_{10}$ of the spectral density of the meridional component of the barotropic velocity at 20°N for (c) expt 3 and (d) expt 4.

and Schlax (1996) presented, from T/P altimeter data, evidence of weak westward penetration of baroclinic Rossby waves in the form of beta-refracted patterns, although no quantitative analysis was carried out to this respect. White et al. (1998) showed evidence of biennial beta-refracted Rossby waves in the Pacific basin from T/P data, but with no quantitative analysis. Kelly and Thompson (2002) showed time–longitude plots of SSH anomalies derived from T/P altimeter data at 8°, 14°, and 20°N: the seasonal cycle and El Niño/La Niña events manifest themselves in terms of baroclinic Rossby waves that are confined in an eastern band whose width appears in agreement with the analysis discussed here (in this study no explicit reference was made to the beta refraction).

The analysis of Fu and Qiu (2002) is very relevant to our model study. The authors considered eight years of T/P altimeter data in the North Pacific Ocean with the seasonal cycle removed. Signatures of coastal Kelvin waves propagating northward from the Tropics and of Rossby waves generated by their passage were clearly revealed. An analysis of the spectral power density of SSH anomaly at 2° offshore from the eastern boundary showed that the radiated baroclinic Rossby waves had, indeed, frequencies lower than the critical value given by (7). Moreover, in order to test the relative impor-

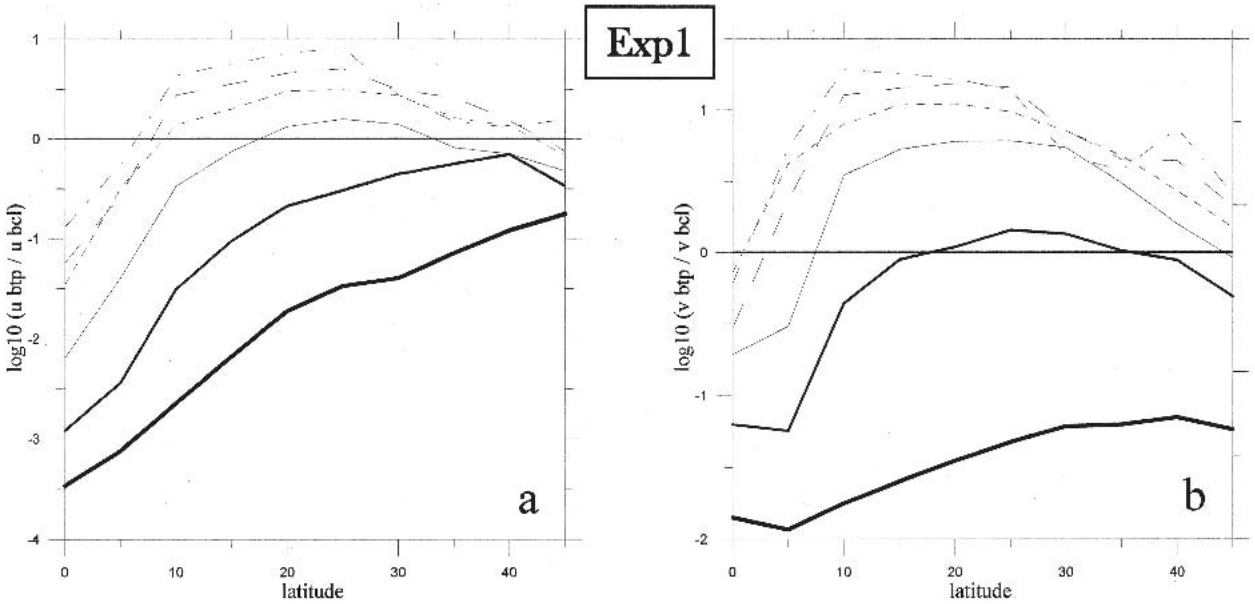

FIG. 9. As in Figs. 5a,b but with spatial integration in Eq. (6) from $x = 500$ km to $x = L - 500$ km.

tance of Rossby waves generated by the wind in mid-ocean and of those generated at the eastern boundary, Fu and Qiu (2002) simulated the boundary-driven waves by integrating the evolution equation of potential vorticity in the quasigeostrophic approximation along the wave characteristics in the x–t plane after prescribing the observed coastal variability as boundary forcing. They then computed the correlation between the simulated boundary-driven Rossby wave SSH signal and the T/P SSH anomaly. The map of the correlation coefficients (Fig. 4a of Fu and Qiu 2002) shows a typical beta-refracted Rossby wave pattern (although no mention was made of this effect), but the correlation, high near the coasts, becomes mostly insignificant in the ocean interior. The authors suggested that the rapid degradation of the correlation offshore might be due to the inadequacy of the model equation used to simulate the boundary-driven Rossby waves.

We believe that this is indeed the case. The quasigeostrophic long-wave equation used by Fu and Qiu (2002) allows only for waves with zonal wave numbers ($k_y = 0$), and this filters out any refraction effect associated with the dependence of wave speed with latitude. In fact, as we have discussed in section 3a, while k_y vanishes for a wave packet lying at the meridional eastern coast, it increases as the wave packet approaches the equator. We conjecture that if the boundary-driven Rossby waves were modeled through an equation that allowed for the refraction, then significant correlation also in the ocean interior might be found, and a striking evidence of beta refraction (already noticeable in the correlation map) would be provided.

In conclusion, several studies based on altimeter data demonstrate the actual existence of beta-refracted baroclinic Rossby waves. However, a systematic study based on altimeter data specifically devoted to analyze quantitative aspects of beta-refracted Rossby waves, such as their confinement from the eastern coast as a function of frequency, and their local and remote equatorial origin (all features discussed in this section) appears to be still lacking. A study of this nature could provide valuable information on the variability of the oceans, particularly within the Tropics.

4. Barotropic Rossby waves reflected at the western boundary

In this section the barotropic boundary-driven variability will be discussed. From Figs. 5a and 5b it emerges that both components of the zonally integrated baroclinic velocity are much larger in amplitude than the corresponding barotropic components at any frequency for $\varphi \leq 5°$. For $\nu \leq 0.02$ cpd the baroclinic velocity is higher than the barotropic velocity at any latitude, whereas the barotropic velocity is predominant for $\nu > 0.02$ cpd for latitudes higher than $\varphi > 5°$. Figure 8 shows the logarithm of the spectral density of the upper-layer baroclinic meridional velocity (Fig. 8a) and of the barotropic velocity (Fig. 8b) at $\varphi = 20°$ for experiment 1. From Fig. 8a (and for Figs. 2d–f as well) it is clear that the zonally integrated meridional baroclinic velocity spectral density includes, for $\nu > \bar{\nu}$, a Kelvin wave signal (the red coastal stripes already discussed in section 3a) that is predominant when compared with the Rossby wave signal. If the Kelvin waves (which have only an alongshore, i.e., in our case a meridional, velocity) are excluded from the zonal integra-

tion [e.g., if the integration is carried out in (6) from $x = 500$ km to $x = L - 500$ km], then the zonally integrated meridional barotropic velocity spectral density associated only with Rossby waves becomes predominant with respect to the baroclinic component also for $\varphi \geq 20°$ and $\nu > 0.01$ cpd, as shown in Fig. 9b (the ratio of the zonal components is virtually unchanged: cf. Fig. 9a with Fig. 5a).

The energy distribution of the barotropic meridional variability at $\varphi = 20°$ (Fig. 8b, but analogous conclusions could be drawn for higher latitudes) is westward confined and intensified and, for frequencies higher than $\nu \approx 0.01$ cpd, the zonal extension of the signal increases as the frequency increases. This westward-confined and -intensified barotropic behavior at high frequencies looks specular with respect the eastward-confined and -intensified baroclinic behavior at low frequencies (Fig. 8a) discussed in section 3. The two underlying dynamics are, obviously, totally different, as we now pass to discuss.

How to interpret the barotropic signal of Fig. 8b? This is compatible with barotropic long Rossby waves generated in midocean and reflected at the western boundary in the form of short waves, whose energy then travels eastward and is selectively damped by the horizontal eddy viscosity. This mechanism is analogous to that proposed by Pedlosky (1965, 1987) in order to explain the western intensification of the currents induced by a constant (in time) wind. In such a theory, the wind introduces into the system energy in a broad range of spatial and temporal scales, and the requirement that the scales be effectively trapped off the western boundary limits them to those that are critically damped, thus allowing the oceanic response to pass from a time-dependent transient state to a steady western boundary current. Here, on the other hand, each Fourier component introduces only one frequency and few spatial scales, no critical damping occurs, and, naturally, the resulting linear forced response has, asymptotically, the same time dependence of the forcing itself. Pierini (1998) analyzed these dynamical aspects in a numerical process study in a midlatitude beta plane, and identified two regimes whose separation is ruled by the parameter Γ, defined as

$$\Gamma \approx \frac{A_H \beta^2}{\omega^3}. \tag{9}$$

For $\Gamma > 1$, the response lies in a viscous range and is in the form of an oscillating Munk layer, whose width is given by the classical formula

$$l \approx \left(\frac{A_H}{\beta}\right)^{1/3}. \tag{10}$$

For higher frequencies such that $\Gamma < 1$, the response lies in an inertial–viscous range and is in the form of westward-intensified short barotropic Rossby waves with eastward group velocity, confined by dissipation within an eastern band of width:

$$l \approx \frac{\omega^4}{A_H \beta^3}. \tag{11}$$

The dashed red line in Fig. 8b (and the same line in Figs. 8c,d) is given by Eqs. (10) and (11) corrected by an empirical factor $\delta = 10$, which better accounts for the effective energy confinement. The actual confinement of the numerical signal agrees well with the theoretical confinement up to $\nu \cong 0.02$ cpd , while for higher frequencies the agreement is limited to the western half of the domain. Numerical runs with single-frequency forcings show that this disagreement is due to a ray focusing toward the equator for high frequencies, which introduces a zonal limitation of the wave field that increases with increasing latitude. This effect is strictly related to the realistic modeling of the Coriolis parameter, and is not included in (11), which was established in a midlatitude beta plane. However, apart from this additional effect of confinement, the good agreement between theoretical and numerical western intensification of the wave field for sufficiently low frequencies confirms the dynamical interpretation given above. Figure 8c shows the same field of Fig. 8b but with the wind stress of experiment 3: the two responses are very similar despite the fact that the wind along the coast in Fig. 8c vanishes. This confirms that the waves are not induced locally by the wind along the coast, but they are rather Rossby waves reflected at the western boundary from waves originating in midocean, where the energy is strong. Last, in Fig. 8d the same case of Fig. 8b is shown when A_H is increased to 10 000 $m^2\ s^{-1}$ (expt 4): again, the dashed red line models properly the distribution of energy, thus obtaining a confirmation that the dynamics is interpreted correctly. It should be noticed that also the bottom friction is known to be an important dissipative effect for barotropic Rossby waves, but in a coarse-resolution model such as the present one (or that considered by Pierini 1998) this effect is overwhelmed by the lateral eddy viscosity, which has to be sufficiently strong to ensure computational stability. Therefore, formulas (9)–(11) may not provide a precise extension within which the waves are trapped, but the qualitative nature of the response is robust in its basic dynamical functioning.

It is worth examining whether westward intensified barotropic Rossby waves that are possibly related to those theoretically examined above have been detected in altimeter data. Kobashi and Kawamura (2001) analyzed variations of the SSH in the Pacific Subtropical Countercurrent using seven years of T/P and *ERS-1–2* altimeter data in the frequency band $\nu = 0.0045$–0.015 cpd ($T = 65$–220 days). Considerable energy was found at those high frequencies mainly in the form of westward-propagating signals, whose spatial distribution (as shown in longitude–time diagrams at $\varphi = 19.5°$, 22°N;

Plate 2 of Kobashi and Kawamura 2001) is strong close to the western boundary and decreases remarkably toward the east in a manner analogous to that shown, for instance, in Figs. 8b–d. Peaks at 95 and 110 days were recognized to lie near the shear modified baroclinic dispersion curve, while higher-frequency peaks (which account for a significant part of the total energy) were associated with barotropic Rossby waves. The westward propagation was conjectured to be due to planetary eddies generated by an internal dynamical mechanism such as baroclinic instability at the Kuroshio Extension, followed by the inverse energy cascade and resulting amplification of the barotropic component. However, this interpretation does not provide any explanation of the observed western intensification (the authors refer to an undefined instability mechanism that may produce the amplification as the disturbances propagate westward). Topographic interactions with the Izu–Mariana Ridge in the westernmost part of the transects may account for the high variability west of 140°E, but no other significant topographic effects are apparent, especially at $\varphi = 22°$N, that may account for the gradual decrease of the amplitude toward the east. Therefore, the explanation of these aspects of the observed variability in terms of damped barotropic Rossby waves reflected at the western boundary could in principle be considered. We believe it would be worth analyzing in further studies the western intensification of the barotropic variability, such as that observed through altimeter data by Kobashi and Kawamura (2001), in relation with the theoretical arguments discussed in this section.

5. Conclusions

In this article a spectral analysis of the boundary-driven, large-scale oceanic variability has been performed in the framework of a process study based on a two-layer primitive equation ocean model. A simple white-noise wind is used to force the system, and a spectroscopic analysis of the zonal and meridional, barotropic and baroclinic velocity components has been carried out. General aspects of the variability at different frequency bands have been recognized to be in the form of boundary-driven waves: they have then been analyzed on the basis of theoretical arguments and in connection with altimeter observations.

In summary:

1) Baroclinic Rossby waves radiating from the eastern boundary of the ocean are found to be generated by the passage of coastal Kelvin waves that are, in turn, generated in the equatorial waveguide by variable winds through a teleconnection mechanism known to act in El Niño events. Moreover, the westward propagation of the waves from the eastern coast produces beta-refracted patterns that yield a spatial confinement of width equal to one wavelength at each frequency (this effect was reproduced by the model thanks to the realistic representation of the Coriolis parameter). In several altimeter data analyses, beta-refraction effects have been observed, but a systematic study based on altimeter data specifically devoted to analyzing the quantitative aspects of beta-refracted boundary-driven baroclinic Rossby waves considered in this article (such as their confinement from the eastern coast as a function of frequency and their remote equatorial origin) appears to be still lacking. It is therefore suggested that such a study could provide valuable information on the oceanic variability, particularly in tropical regions.
2) Barotropic Rossby waves are found to radiate from the western boundary of the ocean after reflection of long westward-propagating barotropic Rossby waves generated in midocean. The short reflected waves are damped during their eastward propagation, so they yield a sort of westward intensification whose quantitative properties are discussed. There is evidence, in altimeter data, of SSH signatures compatible with barotropic Rossby waves that show a gradual decrease in amplitude for increasing distance from the western coast. No clear explanation of this effect is provided, and so it is suggested that an analysis of that aspect of the variability could be performed in view of the numerical results presented here.

Future developments of this model study include a more realistic setup (variable coasts and bottom topography, but always in a schematic framework) and the use of schematic winds inspired by realistic wind fields [as done for the seasonal variability in Pierini (2003)] with the aim of performing simulations of altimeter observations of boundary-driven Rossby waves that can be interpreted theoretically, also on the basis of the results of this paper. Another development concerns the effect that the variability studied in this paper has on the nonlinear properties of the mean wind-driven ocean circulation. An analysis of this nature is currently being carried out in the framework of a generalized double-gyre, reduced-gravity eddy-resolving version of the circulation model used in the present study.

Acknowledgments. This research was supported by the Italian Space Agency (A.S.I.).

REFERENCES

Anderson, D. L. T., and P. W. Rowlands, 1976: The role of inertia–gravity and planetary waves in the response of a tropical ocean to the incidence of an equatorial Kelvin wave on a meridional boundary. *J. Mar. Res.,* **34,** 295–312.

Chelton, D. B., and R. E. Davis, 1982: Monthly mean sea level variability along the west coast of North America. *J. Phys. Oceanogr.,* **12,** 757–784.

——, and M. G. Schlax, 1996: Global observations of oceanic Rossby waves. *Science,* **272,** 234–238.

Cummins, P. F., L. A. Mysak, and K. Hamilton, 1986: Generation of annual Rossby waves in the North Pacific by the wind stress curl. *J. Phys. Oceanogr.,* **16,** 1179–1189.

Fu, L. L., and D. B. Chelton, 2001: Large-scale ocean circulation. *Satellite Altimetry and Earth Sciences,* L. L. Fu and A. Cazenave, Eds., Academic Press, 133–169.

——, and B. Qiu, 2002: Low-frequency variability of the North Pacific Ocean: The roles of boundary- and wind-driven baroclinic Rossby waves. *J. Geophys. Res.,* **107,** 3220, doi:10.1029/2001JC001131.

Herrmann, P., and W. Krauss, 1989: Generation and propagation of annual Rossby waves in the North Atlantic. *J. Phys. Oceanogr.,* **19,** 727–744.

Johnson, M. A., and J. J. O'Brien, 1990a: The northeast Pacific Ocean response to the 1982–83 El Niño. *J. Geophys. Res.,* **95,** 7155–7166.

——, and ——, 1990b: The role of coastal Kelvin waves on the northeast Pacific Ocean. *J. Mar. Syst.,* **1,** 29–38.

Kelly, K. A., and L. Thompson, 2002: Scatterometer winds explain damped Rossby waves. *Geophys. Res. Lett.,* **29,** 1991, doi: 10.1029/2002GL015595.

Kobashi, F., and H. Kawamura, 2001: Variation of sea surface height at periods of 65–220 days in the subtropical gyre of the North Pacific. *J. Geophys. Res.,* **106,** 26 817–26 831.

McCreary, J., 1976: Eastern tropical ocean response to changing wind systems: With application to El Niño. *J. Phys. Oceanogr.,* **6,** 632–645.

Meyers, G., 1979: On the annual Rossby wave in the tropical North Pacific Ocean. *J. Phys. Oceanogr.,* **9,** 663–674.

Pedlosky, J., 1965: A note on the western intensification of the oceanic circulation. *J. Mar. Res.,* **23,** 207–209.

——, 1987: *Geophysical Fluid Dynamics*. Springer-Verlag, 710 pp.

Philander, S. G., 1990: *El Niño, La Niña, and the Southern Oscillation*. Academic Press, 289 pp.

——, and J. H. Yoon, 1982: Eastern boundary currents and coastal upwelling. *J. Phys. Oceanogr.,* **12,** 862–879.

Picaut, J., and A. J. Busalacchi, 2001: Tropical ocean variability. *Satellite Altimetry and Earth Sciences,* L. L. Fu and A. Cazenave, Eds., Academic Press, 217–236.

Pierini, S., 1996: Topographic Rossby modes in the Strait of Sicily. *J. Geophys. Res.,* **101,** 6429–6440.

——, 1997: Westward intensified and topographically modified planetary modes. *J. Phys. Oceanogr.,* **27,** 1459–1471.

——, 1998: Wind-driven fluctuating western boundary currents. *J. Phys. Oceanogr.,* **28,** 2185–2198.

——, 2003: A model of the wind-driven seasonal variability in the tropical North Pacific, with validation through altimeter data. *J. Phys. Oceanogr.,* **33,** 2156–2172.

Qiu, B., W. Miao, and P. Müller, 1997: Propagation and decay of forced and free baroclinic Rossby waves in off-equatorial oceans. *J. Phys. Oceanogr.,* **27,** 2405–2417.

Schopf, P. S., D. L. T. Anderson, and R. Smith, 1981: Beta-dispersion of low-frequency Rossby waves. *Dyn. Atmos. Oceans,* **5,** 187–214.

Soares, J., I. Wainer, and N. C. Wells, 1999: Reflection of equatorial Kelvin waves at eastern ocean boundaries. Part I: Hypothetical boundaries. *Ann. Geophys.,* **17,** 812–826.

Stammer, D., C. Wunsch, and R. M. Ponte, 2000: De-aliasing of global high frequency barotropic motions in altimeter observations. *Geophys. Res. Lett.,* **27,** 1175–1178.

White, W. B., 1977: Annual forcing of baroclinic long waves in the tropical North Pacific Ocean. *J. Phys. Oceanogr.,* **7,** 50–61.

——, and J. F. T. Saur, 1981: A source of annual baroclinic waves in the eastern subtropical North Pacific. *J. Phys. Oceanogr.,* **11,** 1452–1462.

——, Y. Chao, and C. K. Tai, 1998: Coupling of biennial oceanic Rossby waves with the overlying atmosphere in the Pacific basin. *J. Phys. Oceanogr.,* **28,** 1236–1251.